Progress In Electromagnetics Research B, Vol. 76, 59–71, 2017

Data-driven Strategies for Cross-Track Motion Compensation in Synthetic Aperture Radar Imaging

Po-Chih Chen and Jean-Fu Kiang*

Abstract—Nine different strategies are proposed to compensate the cross-track motion errors in synthetic aperture radar (SAR) imaging, based on estimating the phase coefficients of the phase history. A spline interpolation method and a subaperture reconstruction method are used to derive the phase history over the whole aperture, based on the phase coefficients previously estimated. Four different scenarios are designed to compare the performance of these nine strategies.

1. INTRODUCTION

Motion compensation (MOCO) is critical to the quality of airborne synthetic aperture radar (SAR) imaging. The flight path of the platform during a SAR mission is inevitably perturbed by local weather condition, resulting in motion errors that will affect the received signal and deteriorate the imaging quality. The motion information of the platform can be provided, to certain degree of accuracy, by an inertial navigation system (INS) [1] or the global positioning system (GPS) [2]. In [3], the information derived from INS / GPS was used to compensate for the first-order range-independent motion error, and then a reflectivity displacement method (RDM) was applied to estimate the second-order range-dependent residue motion errors.

As an alternative, motion errors can be estimated from the received signal itself [3–13]. In [4], a two-step MOCO approach was implemented on an extended chirp scaling (ECS) algorithm. In the first step, the deviation from a reference point is corrected before range compression. In the second step, a range-dependent phase correction is applied after range compression and RCM correction, before azimuth compression.

In [5], a 3D MOCO method was proposed. First, the instantaneous Doppler rate and the Doppler centroid are estimated by using a subaperture method. Then, the forward velocity and the displacement in the line-of-sight (LOS) direction are extracted from the instantaneous Doppler rate. A weighted least-square (WLS) method was proposed by taking multiple Doppler rate data at different range gates to minimize the error in estimating the acceleration vector. In [6], two coefficients in each azimuth gate are derived from the Doppler rates estimated at all the range gates via a straight-line fitting method, which are then applied to estimate the forward velocity and displacement in the LOS direction.

In conventional two-step MOCO algorithms, along-track motion errors are usually neglected, except when the SAR system operates at a large squint-angle or in a wide-beam mode [7]. In [8], three Fourier-based MOCO algorithms were implemented on range Doppler, extend chirp scaling (ECS) and ωK algorithms. A precise topography and aperture-dependent (PTA) algorithm [9, 10] was applied to correct the residual phase error associated with a target. A subaperture topography and aperture-dependent (SATA) algorithm [7, 8], which is a variant of PTA, implemented MOCO before azimuth compression. A frequency division (FD) algorithm [11, 12], which is similar to SATA, applied subaperture technique in the frequency domain instead of the time domain. In [7], the SATA algorithm was applied after

Received 19 March 2017, Accepted 4 June 2017, Scheduled 14 June 2017
* Corresponding author: Jean-Fu Kiang (jfkiang@ntu.edu.tw).
The authors are with the Graduate Institute of Communication Engineering, National Taiwan University, Taipei, Taiwan, R.O.C.

the standard two-step MOCO. However, SATA can only partially compensate the azimuth-dependent motion errors since the phase is corrected only in the middle of subapertures. The first-order motion error in each subaperture is accounted for by using a scaled Fourier transform (SFT).

In [13], the phase error was attributed to some parameters, including azimuth velocity and radial acceleration, and the problem of motion compensation was converted to the estimation of these parameters. The whole aperture was divided into multiple subapertures, with the motion parameters approximated as constants in each subaperture.

In this work, the phase history is expanded in a Taylor's series up to the third-order terms, as compared to the second-order terms in [5, 6]. The whole aperture is divided into multiple subapertures, and the phase coefficients are estimated at the middle of each subaperture. A spline interpolation method and a subaperture reconstruction method are proposed to derive the temporal profiles of phase coefficients over the whole aperture. Nine strategies are then proposed to compensate the motion error, and four different scenarios are designed to analyze and compare the performance of these strategies.

This work is organized as follows. A polynomial representation of phase history is presented in Section 2, in an airborne zero-squint SAR mission; three models for estimating the phase coefficients in subapertures are presented in Section 3; two methods to derive the slow-time profiles of phase coefficients over the whole aperture are presented in Section 4; nine strategies for cross-track MOCO are proposed in Section 5. Four simulation scenarios are described in Section 6; imaging performance of these nine strategies in these four scenarios are compared and discussed in Section 7. Finally, some conclusions are drawn in Section 8.

2. POLYNOMIAL REPRESENTATION OF PHASE HISTORY

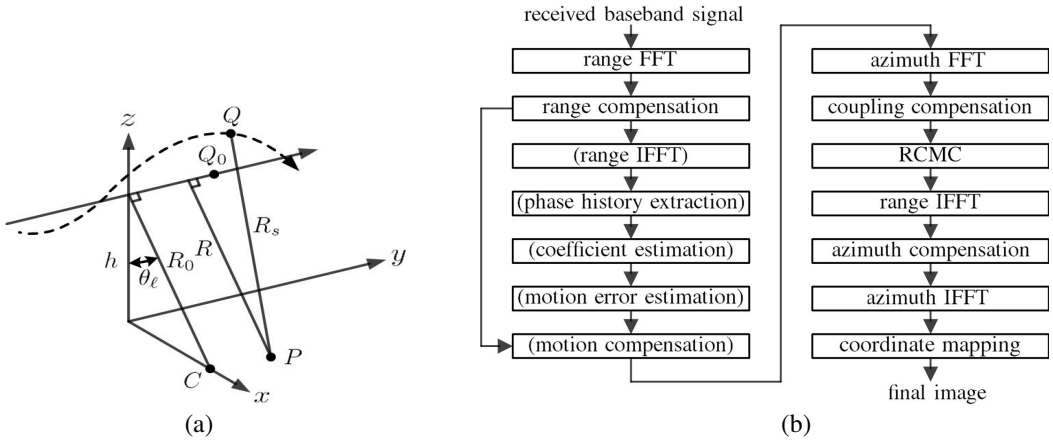

Figure 1. (a) Flight path of a SAR platform with a look angle θ_ℓ towards the target area, solid line: ideal flight path, dashed curve: actual flight path. (b) Flowchart of MOCO, based on a conventional RDA. The processes enclosed with parentheses are designed for MOCO.

Figure 1(a) shows the flight path of a SAR platform with a look angle θ_ℓ towards the target area, where the solid line and the dashed curve represent the ideal and the actual flight paths, respectively. The ideal and the actual position of antenna phase center (APC) at azimuth time η are denoted as $Q_0(0, V_p\eta, h)$ and $Q(x(\eta), y(\eta), z(\eta))$, respectively. The motion error vector, which is the difference between the actual flight path and the ideal one, is $(x(\eta), y(\eta) - V_p\eta, z(\eta) - h)$, where $x(\eta)$ and $z(\eta) - h$ are the cross-track motion errors and $y(\eta) - V_p\eta$ is the along-track motion error. In this work, the squint angle is set to zero and the target area is assumed to be a flat surface. The beam center point (BCP) is at $C(x_c, 0, 0)$, with $x_c = h\tan\theta_\ell$. The range from the BCP to the ideal flight path is $R_0 = \sqrt{x_c^2 + h^2}$. The slant ranges from a point target at $P(x_p, y_p, 0)$ to the actual and the ideal flight paths are $R_s(\eta) = \sqrt{[x(\eta) - x_p]^2 + [y(\eta) - y_p]^2 + z^2(\eta)}$, and $R = \sqrt{x_p^2 + h^2}$, respectively. If the motion

errors are small, the slant range can be approximated as

$$R_s(\eta) \simeq R + \frac{[y(\eta) - y_p]^2}{2R} - x(\eta)\sin\theta_\ell + [z(\eta) - h]\cos\theta_\ell \tag{1}$$

which is composed of an along-track component and two cross-track components.

Figure 1(b) shows the flowchart of implementing motion compensation (MOCO), based on a conventional range-Doppler algorithm (RDA). The transmitted linear frequency modulation (LFM) signal is expressed as $s_t(\tau) = w_e(\tau)e^{j2\pi f_0\tau + j\pi K_r\tau^2}$, where f_0 is the carrier frequency, K_r is the FM rate, τ is the range (fast) time, $w_e(\tau) = \mathrm{rect}(\tau/T_r)$ is the range envelope with duration T_r, and $\mathrm{rect}(\tau)$ is a rectangular function, which equals one when $|\tau| \le 1/2$ and zero otherwise. The received signal scattered from the point target at $P(x_p, y_p, 0)$ is first demodulated, then Fourier transformed with respect to τ to become

$$S_{\mathrm{rb}}(f_\tau, \eta) = b_1 A_0 e^{-j4\pi f_0 R_s(\eta)/c} w_e(f_\tau/K_r) e^{-j\pi f_\tau^2/K_r} e^{-j4\pi f_\tau R_s(\eta)/c} \tag{2}$$

where A_0 is a complex amplitude, which is set to one. The radiation pattern of the SAR radar towards the point target is approximated as one, and b_1 is a constant of integration. Next, the signal in Eq. (2) is multiplied with a range compensation filter $H_{\mathrm{rc}}(f_\tau, \eta) = e^{j\pi f_\tau^2/K_r}$, then inverse Fourier transformed, with respect to f_τ, to obtain

$$s_{\mathrm{rc}}(\tau, \eta) = b_1 A_0 e^{-j4\pi R_s(\eta)/\lambda_0} K_r T_r \mathrm{sinc}\{K_r T_r[\tau - 2R_s(\eta)/c]\} \tag{3}$$

where $\mathrm{sinc}(\alpha) = \sin(\pi\alpha)/(\pi\alpha)$. The phase in Eq. (3) at $\tau - 2R_s(\eta)/c$ is called the phase history, with the explicit form

$$\phi(\eta) = -4\pi R_s(\eta)/\lambda_0 \tag{4}$$

The peak amplitude of $s_{\mathrm{rc}}(\tau, \eta)$ in the τ domain occurs at $\tau'(\eta) = \max_\tau\{|s_{\mathrm{rc}}(\tau, \eta)|\}$, at which $s_{\mathrm{rc}}(\tau, \eta)$ is reduced to

$$s(\eta) = s_{\mathrm{rc}}(\tau'(\eta), \eta) \simeq b_2 e^{j\phi(\eta)} \tag{5}$$

where $b_2 = b_1 A_0 K_r T_r$.

The whole azimuth aperture is divided into S subapertures, each containing N_s azimuth samples. The signal $s(\eta)$ and its phase history $\phi(\eta)$ are represented in these S subapertures as

$$s(\eta) = [s_1(\eta), s_2(\eta), \ldots, s_s(\eta), \ldots, s_S(\eta)], \qquad \phi(\eta) = [\phi_1(\eta), \phi_2(\eta), \ldots, \phi_s(\eta), \ldots, \phi_S(\eta)]$$

with $s_s(\eta) = b_2 e^{j\phi_s(\eta)}$. In the sth subaperture, $\eta_{sb} \le \eta \le \eta_{se}$, $\phi_s(\eta)$ can be approximated by a Taylor's series as

$$\phi_s(\eta) \simeq c_s + \alpha_s(\eta - \eta_s) + \beta_s(\eta - \eta_s)^2 + \gamma_s(\eta - \eta_s)^3 \tag{6}$$

where $\eta_s = (\eta_{sb} + \eta_{se})/2$, $c_s = \phi_s(\eta_s)$, $\alpha_s = \phi_s'(\eta_s)$, $\beta_s = \phi_s''(\eta_s)/2$ and $\gamma_s = \phi_s'''(\eta_s)/6$. The corresponding signal can thus be represented as

$$s_s(\eta) \simeq b_2 e^{j\left[c_s + \alpha_s(\eta-\eta_s) + \beta_s(\eta-\eta_s)^2 + \gamma_s(\eta-\eta_s)^3\right]} \tag{7}$$

By substituting the expression of $R_s(\eta)$ in Eq. (1) into Eq. (6), we have

$$c_s = -\frac{4\pi}{\lambda_0}\left\{R + \frac{[y(\eta_s) - y_p]^2}{2R} - x(\eta_s)\sin\theta_\ell + [z(\eta_s) - h]\cos\theta_\ell\right\} \tag{8}$$

$$\alpha_s = -\frac{4\pi[y(\eta_s) - y_p]v_y(\eta_s)}{\lambda_0 R} + \frac{4\pi v_r(\eta_s)}{\lambda_0} \tag{9}$$

$$\beta_s = -\frac{2\pi v_y^2(\eta_s)}{\lambda_0 R} - \frac{2\pi[y(\eta_s) - y_p]a_y(\eta_s)}{\lambda_0 R} + \frac{2\pi a_r(\eta_s)}{\lambda_0} \tag{10}$$

$$\gamma_s = -\frac{2\pi v_y(\eta_s)a_y(\eta_s)}{\lambda_0 R} - \frac{2\pi[y(\eta_s) - y_p]b_y(\eta_s)}{3\lambda_0 R} + \frac{2\pi b_r(\eta_s)}{3\lambda_0} \tag{11}$$

where the radial kinematic parameters of the platform are expressed as

$$v_r(\eta) = v_x(\eta)\sin\theta_\ell - v_z(\eta)\cos\theta_\ell, \qquad a_r(\eta) = a_x(\eta)\sin\theta_\ell - a_z(\eta)\cos\theta_\ell$$

$$b_r(\eta) = \frac{da_r(\eta)}{d\eta} = b_x(\eta)\sin\theta_\ell - b_z(\eta)\cos\theta_\ell$$

with $b_x(\eta) = da_x(\eta)/d\eta$ and $b_z(\eta) = da_z(\eta)/d\eta$.

3. ESTIMATION OF PHASE COEFFICIENTS IN SUBAPERTURES

Three different models are proposed to represent the phase history in each subaperture.

3.1. First-Order Model

If only the first-order term in the phase history is considered, Eq. (7) is reduced to

$$s_s(\eta) \simeq b_3 e^{j\alpha_s \eta} \tag{12}$$

where $b_3 = b_2 e^{j(c_s - \alpha_s \eta_s)}$. By taking the Fourier transform of the signal in Eq. (12) with respect to η, we obtain

$$S_s(f_\eta) \simeq b_3 T_a \text{sinc}\left\{[f_\eta - \alpha_s/(2\pi)]T_a\right\} \tag{13}$$

where $T_a = N_a \Delta\eta$ is the synthetic aperture time span. Eq. (13) implies that a peak occurs at $f_{\eta p1} = \tilde{\alpha}_s/(2\pi)$. Hence α_s is estimated as $\tilde{\alpha}_s = 2\pi f_{\eta p1}$.

3.2. Second-Order Model

If the phase history is expanded up to the second-order term, Eq. (7) is reduced to

$$s_s(\eta) \simeq b_4 e^{j\left(\alpha_s' \eta + \beta_s \eta^2\right)} \tag{14}$$

where $b_4 = b_3 e^{j\beta_s \eta_s^2}$ and $\alpha_s' = \alpha_s - 2\beta_s \eta_s$. Define a product $w(\eta, \eta') = s_s^*(\eta) s_s(\eta + \eta') = b_5 e^{j2\beta_s \eta' \eta}$, where $b_5 = b_4 b_4^* e^{j\left(\alpha_s' \eta' + \beta_s \eta'^2\right)}$. The Fourier transform of $w(\eta, \eta')$ with respect to η is $W(f_\eta, \eta') = b_5 T_a \text{sinc}\left[(f_\eta - \beta_s \eta'/\pi)T_a\right]$, in which a peak occurs at $f_{\eta p2} = \tilde{\beta}_s \eta'/\pi$. Thus, β_s is estimated as $\tilde{\beta}_s = \pi f_{\eta p2}/\eta'$. By multiplying a second-order compensation filter $H_{c2}(\eta) = e^{-j\tilde{\beta}_s(\eta - \eta_s)^2}$ to the signal in Eq. (14), we obtain

$$s_s'(\eta) = s_s(\eta) H_{c2}(\eta) = b_2 e^{j\left[c_s + \alpha_s(\eta - \eta_s) + (\beta_s - \tilde{\beta}_s)(\eta - \eta_s)^2\right]} \simeq b_2 e^{j[c_s + \alpha_s(\eta - \eta_s)]} \tag{15}$$

of which the phase is a linear function of η, as in Eq. (12).

3.3. Third-Order Model

If the phase history is expanded up to the third-order term, Eq. (7) is rewritten as

$$s_s(\eta) \simeq b_6 e^{j\left(\alpha_s'' \eta + \beta_s' \eta^2 + \gamma_s \eta^3\right)} \tag{16}$$

where $b_6 = b_4 e^{-j\gamma_s \eta_s^3}$, $\alpha_s'' = \alpha_s' + 3\gamma_s \eta_s^2$ and $\beta_s' = \beta_s - 3\gamma_s \eta_s$. Define a product $w_1(\eta, \eta') = s_s^*(\eta) s_s(\eta + \eta') = b_7 e^{j\beta_s'' \eta + j\gamma_s' \eta^2}$, where $b_7 = b_6 b_6^* e^{j\left(\alpha_s'' \eta' + \beta_s' \eta'^2 + \gamma_s \eta'^3\right)}$, $\beta_s'' = 2\beta_s' \eta' + 3\gamma_s \eta'^2$ and $\gamma_s' = 3\gamma_s \eta'$. Next, derive another product $w_2(\eta, \eta', \eta'') = w_1^*(\eta, \eta') w_1(\eta + \eta'', \eta') = b_8 e^{j2\gamma_s' \eta'' \eta}$, where $b_8 = b_7 b_7^* e^{j\left(\beta_s'' \eta'' + \gamma_s' \eta''^2\right)}$. By taking the Fourier transform of $w_2(\eta, \eta', \eta'')$ with respect to η, we obtain $W_2(f_\eta, \eta', \eta'') = b_8 T_a \text{sinc}\left[(f_\eta - \gamma_s' \eta''/\pi)T_a\right]$, in which a peak occurs at $f_{\eta p3} = \tilde{\gamma}_s' \eta''/\pi$. Thus, γ_s' is estimated as $\tilde{\gamma}_s' = \pi f_{\eta p3}/\eta''$, and γ_s is estimated as $\tilde{\gamma}_s = \tilde{\gamma}_s'/(3\eta')$. By multiplying a third-order compensation filter $H_{c3}(\eta) = e^{-j\tilde{\gamma}_s(\eta - \eta_s)^3}$ to the signal in Eq. (16), we obtain

$$s_s''(\eta) = s_s(\eta) H_{c3}(\eta) = b_2 e^{j\left[c_s + \alpha_s(\eta - \eta_s) + \beta_s(\eta - \eta_s)^2 + (\gamma_s - \tilde{\gamma}_s)(\eta - \eta_s)^3\right]} \simeq b_2 e^{j\left[c_s + \alpha_s(\eta - \eta_s) + \beta_s(\eta - \eta_s)^2\right]} \tag{17}$$

of which the phase is a quadratic function of η, as in Eq. (14).

4. SLOW-TIME PROFILES OF PHASE COEFFICIENTS

An interpolation method and a reconstruction method are proposed to derive the slow-time profile of each phase coefficient over the whole aperture, based on the phase coefficients estimated in the last Section.

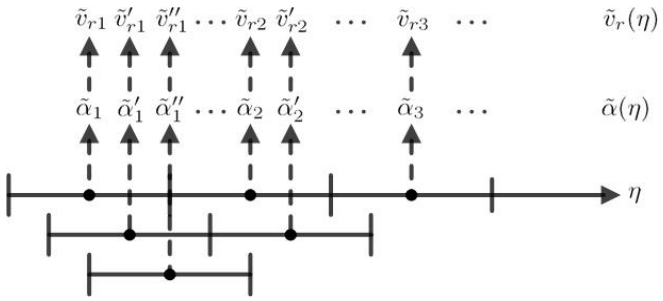

Figure 2. Schematic of estimating $\tilde{\alpha}'(\eta)$ between centers of subapertures.

4.1. Interpolation Method

The phase history at each slow-time instant can be expanded in the same form as Eq. (6), and the coefficient α_s will become a function of η. Fig. 2 shows the schematic of estimating $\tilde{\alpha}(\eta)$. Intuitively, by shifting the original sth subaperture an integer number of $\Delta\eta$, a new subaperture is formed, having a new coefficient $\tilde{\alpha}'_s$ at its center. The new coefficient $\tilde{\alpha}'_s$ changes continuously from α_s to α_{s+1} as the sth subaperture is shifted gradually by 0 to $N_s\Delta\eta$. Thus, a spline interpolation method is applied to derive the slow-time profile $\tilde{\alpha}(\eta)$ from coefficients $\tilde{\alpha}_s$'s at the centers of the original subapertures.

4.2. Reconstruction Method

The coefficient $\alpha(\eta)$ in $\eta_{sb} \le \eta \le \eta_{se}$ can be expanded into a Taylor's series, centered at η_s, as

$$\hat{\alpha}_s(\eta) \simeq \alpha_s + \left.\frac{d^2\phi_s(\eta)}{d\eta^2}\right|_{\eta=\eta_s}(\eta-\eta_s) + \frac{1}{2}\left.\frac{d^3\phi_s(\eta)}{d\eta^3}\right|_{\eta=\eta_s}(\eta-\eta_s)^2 \simeq \tilde{\alpha}_s + 2\tilde{\beta}_s(\eta-\eta_s) + 3\tilde{\gamma}_s(\eta-\eta_s)^2 \quad (18)$$

Similarly, $\beta(\eta)$ in $\eta_{sb} \le \eta \le \eta_{se}$ can be expanded as

$$\hat{\beta}_s(\eta) \simeq \beta_s + \left.\frac{d}{d\eta}\left[\frac{1}{2}\frac{d^2\phi_s(\eta)}{d\eta^2}\right]\right|_{\eta=\eta_s}(\eta-\eta_s) = \tilde{\beta}_s + 3\tilde{\gamma}_s(\eta-\eta_s) \quad (19)$$

5. STRATEGIES FOR CROSS-TRACK MOCO

In this work, along-track motion error is neglected, which implies that $y(\eta) = V_p\eta$, $v_y(\eta) = V_p$ and $a_y(\eta) = b_y(\eta) = 0$. To correct the cross-track motion errors, a MOCO filter is applied, which is represented as

$$H_{\rm ct}(f_\tau, \eta) = e^{-j4\pi(f_0+f_\tau)\Delta R(\eta)/c} \quad (20)$$

where $\Delta R(\eta)$ is the motion error in the radial direction, which will be estimated from the received signal.

Figure 3 lists nine strategies for motion-error estimation. The roman numeral indicates the order of model used to estimate the phase coefficients, and the arabic numeral indicates the order of phase coefficient chosen for motion-error estimation. Strategies initial with roman numeral and R indicates the use of interpolation method and reconstruction method, respectively, to derive the slow-time profile of phase coefficients over the aperture.

5.1. Strategies I-1, II-1, III-1, R-1 and R-2

The radial velocity of the platform is derived by using Eq. (9) as

$$\tilde{v}_r(\eta) = \frac{\lambda_0}{4\pi}\left[\tilde{\alpha}(\eta) + \frac{4\pi(V_p\eta - y_p)V_p}{\lambda_0 R}\right] \quad (21)$$

I-1 $\{\tilde{\alpha}_s\}_{\mathrm{I}} \longrightarrow \tilde{\alpha}(\eta) \longrightarrow \tilde{v}_r(\eta) \longrightarrow \Delta R_1(\eta)$
II-1 $\{\tilde{\alpha}_s\}_{\mathrm{II}} \longrightarrow \tilde{\alpha}(\eta) \longrightarrow \tilde{v}_r(\eta) \longrightarrow \Delta R_2(\eta)$
II-2 $\{\tilde{\beta}_s\}_{\mathrm{II}} \longrightarrow \tilde{\beta}(\eta) \longrightarrow \tilde{a}_r(\eta) \longrightarrow \tilde{v}_r(\eta) \longrightarrow \Delta R_3(\eta)$
III-1 $\{\tilde{\alpha}_s\}_{\mathrm{III}} \longrightarrow \tilde{\alpha}(\eta) \longrightarrow \tilde{v}_r(\eta) \longrightarrow \Delta R_4(\eta)$
III-2 $\{\tilde{\beta}_s\}_{\mathrm{III}} \longrightarrow \tilde{\beta}(\eta) \longrightarrow \tilde{a}_r(\eta) \longrightarrow \tilde{v}_r(\eta) \longrightarrow \Delta R_5(\eta)$
III-3 $\{\tilde{\gamma}_s\}_{\mathrm{III}} \longrightarrow \tilde{\gamma}(\eta) \longrightarrow \tilde{b}_r(\eta) \longrightarrow \tilde{a}_r(\eta) \longrightarrow \tilde{v}_r(\eta) \longrightarrow \Delta R_6(\eta)$
R-1 $\{\tilde{\alpha}_s, \tilde{\beta}_s\}_{\mathrm{II}} \longrightarrow \hat{\alpha}(\eta) \longrightarrow \tilde{v}_r(\eta) \longrightarrow \Delta R_7(\eta)$
R-2 $\{\tilde{\alpha}_s, \tilde{\beta}_s, \tilde{\gamma}_s\}_{\mathrm{III}} \longrightarrow \hat{\alpha}(\eta) \longrightarrow \tilde{v}_r(\eta) \longrightarrow \Delta R_8(\eta)$
R-3 $\{\tilde{\beta}_s, \tilde{\gamma}_s\}_{\mathrm{III}} \longrightarrow \hat{\beta}(\eta) \longrightarrow \tilde{a}_r(\eta) \longrightarrow \tilde{v}_r(\eta) \longrightarrow \Delta R_9(\eta)$

Figure 3. Nine strategies for motion-error estimation.

Then, the motion error in the radial direction is derived by integrating $\tilde{v}_r(\eta)$ over η as

$$\Delta R(\eta) = \int_{\eta_b}^{\eta} \tilde{v}_r(s)ds + \Delta R(\eta_b) \tag{22}$$

where $\Delta R(\eta_b)$ is the motion error at $\eta = \eta_b$, the initial azimuth time of the first subaperture. Note that the magnitude of $\tilde{\alpha}(\eta)$ in strategy I-1 is different from that in strategies II-1 or III-1 and that of $\hat{\alpha}(\eta)$ in strategies R-1 or R-2.

5.2. Strategies II-2, III-2 and R-3

The radial acceleration of the platform is derived by using Eq. (10) as

$$\tilde{a}_r(\eta) \simeq \frac{\lambda_0}{2\pi}\left[\tilde{\beta}(\eta) + \frac{2\pi V_p^2}{\lambda_0 R}\right] \tag{23}$$

Then, the velocity error in the radial direction is derived by integrating $\tilde{a}_r(\eta)$ over η as

$$\tilde{v}_r(\eta) = \int_{\eta_b}^{\eta} \tilde{a}_r(s)ds + v_r(\eta_b) \tag{24}$$

where $v_r(\eta_b)$ is the radial velocity of the platform at $\eta = \eta_b$. By using Eqs. (22) and (24), the motion error in the radial direction is derived as

$$\Delta R(\eta) = \int_{\eta_b}^{\eta} \tilde{v}_r(s)ds + \Delta R(\eta_b) = \int_{\eta_b}^{\eta}\left[\int_{\eta_b}^{s} \tilde{a}_r(u)du + v_r(\eta_b)\right]ds + \Delta R(\eta_b) \tag{25}$$

Note that the magnitude of $\tilde{\beta}(\eta)$ in strategy II-2 is different from that in strategy III-2 and that of $\hat{\beta}(\eta)$ in strategy R-3.

5.3. Strategy III-3

The radial acceleration rate of the platform is derived by using Eq. (11) as

$$\tilde{b}_r(\eta) \simeq \frac{3\lambda_0}{2\pi}\tilde{\gamma}(\eta) \tag{26}$$

Then, the acceleration error in the radial direction is derived by integrating $\tilde{b}_r(\eta)$ over η as

$$\tilde{a}_r(\eta) = \int_{\eta_b}^{\eta} \tilde{b}_r(s)ds + a_r(\eta_b) \tag{27}$$

where $a_r(\eta_b)$ is the radial acceleration of the platform at $\eta = \eta_b$. By using Eqs. (25) and (27), the motion error in the radial direction is derived as

$$\begin{aligned}\Delta R(\eta) &= \int_{\eta_b}^{\eta}\left[\int_{\eta_b}^{s} \tilde{a}_r(u)du + v_r(\eta_b)\right]ds + \Delta R(\eta_b) \\ &= \int_{\eta_b}^{\eta}\left\{\int_{\eta_b}^{s}\left[\int_{\eta_b}^{u} \tilde{b}_r(w)dw + a_r(\eta_b)\right]du + v_r(\eta_b)\right\}ds + \Delta R(\eta_b)\end{aligned} \tag{28}$$

6. SIMULATION SCENARIOS

Table 1 lists the parameters used in the simulations [14], where $\alpha_{os} = 8$ is the oversampling ratio. Four different scenarios are considered as follows.

Table 1. Parameters of SAR mission [14].

parameter	symbol	magnitude	unit	parameter	symbol	magnitude	unit
effective radar velocity	V_p	150	m/s	azimuth sampling rate	F_a	300 $\times\alpha_{os}$	Hz
carrier frequency	f_0	10	GHz	azimuth sampling interval	$\Delta\eta$	3.33 $/\alpha_{os}$	ms
chirp pulse duration	T_r	1	μs	number of azimuth samples	N_a	256 $\times\alpha_{os}$	
range chirp rate	K_r	300	THz/s	number of subapertures	S	16	
bandwidth	B_r	300	MHz	height of the platform	h	3	km
range sampling rate	F_r	660 $\times\alpha_{os}$	MHz	look angle	θ_ℓ	53	deg.
range sampling interval	$\Delta\tau$	1.52 $/\alpha_{os}$	ns	squint angle	θ_s	0	deg.
number of range samples	N_r	1,024 $\times\alpha_{os}$					

6.1. Scenario S_1: $db_r/d\eta \neq 0$

The tip of motion-error vector moves in the xz plane along a circle of radius r_s, at a frequency of f_s, leading to a track

$$\begin{bmatrix} x(\eta) \\ y(\eta) \\ z(\eta) \end{bmatrix} = \begin{bmatrix} 0 \\ V_p\eta \\ h \end{bmatrix} + \begin{bmatrix} r_s\cos(2\pi f_s\eta) \\ 0 \\ r_s\sin(2\pi f_s\eta) \end{bmatrix} \tag{29}$$

The associated kinetic parameters in the radial direction are

$$\begin{aligned} v_r(\eta) &= 2\pi f_s r_s\left[-\sin(2\pi f_s\eta)\sin\theta_\ell - \cos(2\pi f_s\eta)\cos\theta_\ell\right] \\ a_r(\eta) &= 4\pi^2 f_s^2 r_s\left[-\cos(2\pi f_s\eta)\sin\theta_\ell + \sin(2\pi f_s\eta)\cos\theta_\ell\right] \\ b_r(\eta) &= 8\pi^3 f_s^3 r_s\left[\sin(2\pi f_s\eta)\sin\theta_\ell + \cos(2\pi f_s\eta)\cos\theta_\ell\right] \end{aligned}$$

6.2. Scenario S_2: $da_r/d\eta \neq 0$, $db_r/d\eta = 0$

The motion error increases in the x direction at a constant acceleration rate B_1, leading to a track

$$\begin{bmatrix} x(\eta) \\ y(\eta) \\ z(\eta) \end{bmatrix} = \begin{bmatrix} 0 \\ V_p\eta \\ h \end{bmatrix} + \begin{bmatrix} B_1\eta^3/6 \\ 0 \\ 0 \end{bmatrix} \tag{30}$$

The associated kinetic parameters in the radial direction are

$$v_r(\eta) = B_1\eta^2\sin\theta_\ell/2, \qquad a_r(\eta) = B_1\eta\sin\theta_\ell, \qquad b_r(\eta) = B_1\sin\theta_\ell$$

6.3. Scenario S_3: $dv_r/d\eta \neq 0$, $da_r/d\eta = 0$

The motion error increases in the x direction has a constant acceleration A_1, leading to a track

$$\begin{bmatrix} x(\eta) \\ y(\eta) \\ z(\eta) \end{bmatrix} = \begin{bmatrix} 0 \\ V_p\eta \\ h \end{bmatrix} + \begin{bmatrix} A_1\eta^2/2 \\ 0 \\ 0 \end{bmatrix} \tag{31}$$

The associated kinetic parameters in the radial direction are

$$v_r(\eta) = A_1\eta\sin\theta_\ell, \qquad a_r(\eta) = A_1\sin\theta_\ell, \qquad b_r(\eta) = 0$$

6.4. Scenario S_4: $dv_r/d\eta = 0$

The motion error increases in the x direction at a constant velocity V_1, leading to a track

$$\begin{bmatrix} x(\eta) \\ y(\eta) \\ z(\eta) \end{bmatrix} = \begin{bmatrix} 0 \\ V_p\eta \\ h \end{bmatrix} + \begin{bmatrix} V_1\eta \\ 0 \\ 0 \end{bmatrix} \tag{32}$$

The associated kinetic parameters in the radial direction are

$$v_r(\eta) = V_1\sin\theta_\ell, \qquad a_r(\eta) = b_r(\eta) = 0$$

6.5. Magnitude of Kinetic Parameters

Proper kinetic parameters will be chosen in the simulations, comparable to the data found in the literatures. In [5], the radial acceleration ranged from -0.3 to $0.3\,\mathrm{m/s^2}$. In [6], the motion error ranged from -5 to 5 m, and the radial acceleration ranged from -0.25 to $0.15\,\mathrm{m/s^2}$. In [13], the motion error ranged from -0.2 to 0.2 m. The whole aperture was divided into five subapertures, with the radial accelerations of 0.3, -0.3, -0.2, 0.2 and $0.1\,\mathrm{m/s^2}$, respectively. In [15], the motion error in the x direction followed a sinusoidal from with an amplitude of 3 m. In [16], two different track drifts of 0.7 and 1.23 m, respectively, per 100 m were assumed. In [17], the motion error ranged from -0.1 to 0.1 m. In [14], the motion error followed the form of $\Delta R(\eta) = 0.2\cos(\pi\eta/2)$ m, with x and z components of $\Delta R_x(\eta) = \Delta R\cos(\pi/3)$ and $\Delta R_z(\eta) = \Delta R\sin(\pi/3)$, respectively.

Referred to these data, the radius and rotating frequency in scenario S_1 are chosen as $r_s = 0.2$ m and $f_s = 2$ Hz, respectively. The kinetic parameters in scenarios S_2 to S_4 are determined, comparable to those in scenario S_1, as

$$b_r(\eta)|_{S_2} = \max\{|b_r(\eta)|\}_{S_1}, \qquad a_r(\eta)|_{S_3} = \max\{|a_r(\eta)|\}_{S_1}, \qquad v_r(\eta)|_{S_4} = \max\{|v_r(\eta)|\}_{S_1}$$

leading to $B_1 = 8\pi^3 f_s^3 r_s/\sin\theta_\ell = 496.95$, $A_1 = 4\pi^2 f_s^2 r_s/\sin\theta_\ell = 39.55$ and $V_1 = 2\pi f_s r_s/\sin\theta_\ell = 3.15$.

7. SIMULATION RESULTS AND DISCUSSIONS

Figure 4 shows the reconstructed images in scenario S_1, with strategies I-1, II-1 and III-1, respectively. These three images reveal similar characteristics in the x direction, but distinct characteristics in the y direction. The other six strategies also reveal similar characteristics in the x direction.

Figure 5 shows the profiles along y axis of the reconstructed images in scenario S_1, with the proposed nine strategies. Strategy I-1, based on the first-order model of phase coefficient, does not work well. With strategy III-3, the motion error is obtained by triple integration of $\tilde{\gamma}(\eta)$, and the poor result may be attributed to the accumulation error. In general, higher-order model of phase coefficients can estimate the motion error more accurately, at the cost of more computational load. Hence, strategy III-1 outperforms strategy II-1, and the latter outperforms strategy I-1. Similarly, strategy R-2 performs better than strategy R-1. The result with strategy III-2 is close to that with strategy II-2.

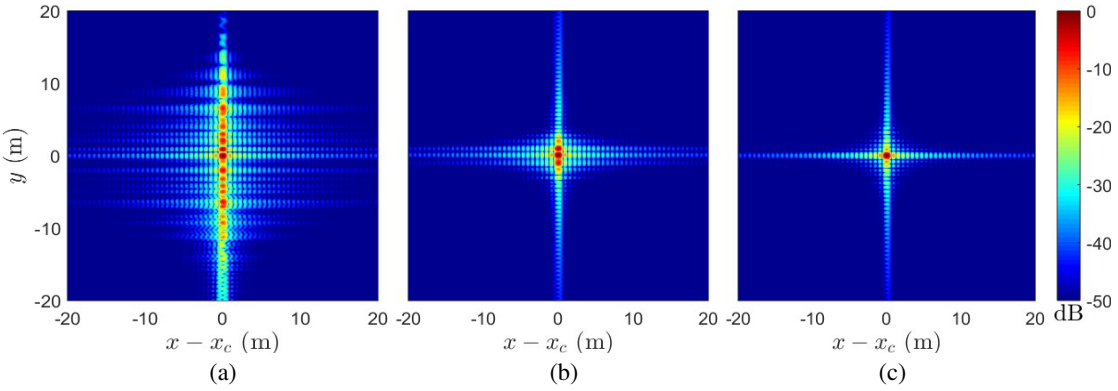

Figure 4. Reconstructed images in scenario S_1 with strategy (a) I-1, (b) II-1 and (c) III-1.

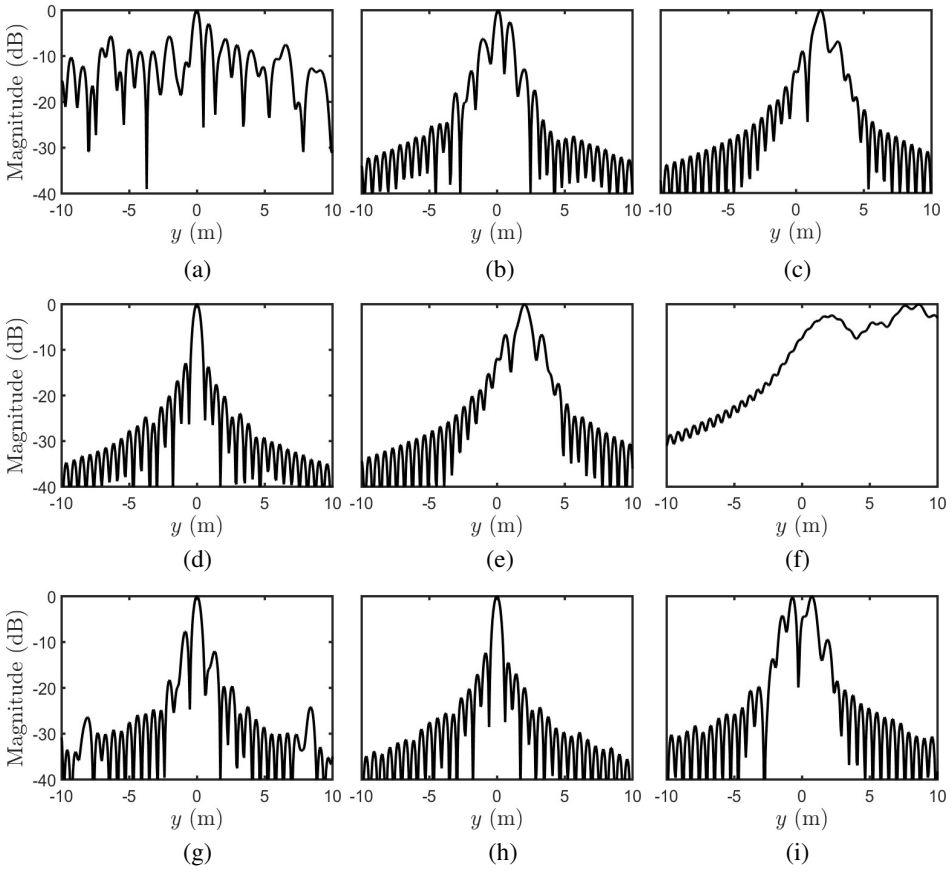

Figure 5. Profiles along y axis of the reconstructed images in scenario S_1, with strategy (a) I-1, (b) II-1, (c) II-2, (d) III-1, (e) III-2, (f) III-3, (g) R-1, (h) R-2 and (i) R-3.

Table 2 lists the performance indices of the reconstructed images with all the proposed nine strategies, where the impulse response width (IRW) is defined as the separation between the two half-power points on both sides of the peak-intensity point; the peak sidelobe ratio (PSLR) is defined as the ratio of the peak intensity to that of the strongest sidelobe; the integrated sidelobe ratio (ISLR) is defined as the ratio of energy in the main lobe to that in all the sidelobes; and the target offset (TO) is defined as the offset of the peak position in the reconstructed image from that of the actual point target.

Table 2. Performance indices of different strategies.

	I-1	II-1	II-2	III-1	III-2	III-3	R-1	R-2	R-3	unit
scenario S_1: $\mathrm{IRW}_x \simeq 0.555\,\mathrm{m}$, $\mathrm{PSLR}_x \simeq -13.243\,\mathrm{dB}$, $\mathrm{ISLR}_x \simeq -9.681\,\mathrm{dB}$, $\mathrm{TO}_x \simeq 0.018\,\mathrm{m}$										
IRW_y	0.496	0.487	0.723	0.516	0.766	2.051	0.509	0.515	0.594	m
PSLR_y	−2.952	−2.656	−6.801	−12.927	−6.664	−0.051	−7.717	−12.35	−0.192	dB
ISLR_y	4.874	−0.122	−4.369	−9.471	−4.601	4.734	−5.807	−9.439	1.252	dB
TO_y	−0.031	0.094	1.781	−0.031	2.031	17.531	−0.031	−0.031	0.719	m
scenario S_2: $\mathrm{IRW}_x \simeq 0.555\,\mathrm{m}$, $\mathrm{PSLR}_x \simeq -13.244\,\mathrm{dB}$, $\mathrm{ISLR}_x \simeq -9.679\,\mathrm{dB}$, $\mathrm{TO}_x \simeq 0.018\,\mathrm{m}$										
IRW_y	3.495	0.514	1.641	0.515	0.514	1.672	0.514	0.515	0.514	m
PSLR_y	−0.01	−12.058	−0.875	−12.508	−13.109	−3.728	−12.259	−12.51	−13.111	dB
ISLR_y	8.584	−9.542	1.283	−9.59	−9.797	3.1	−8.744	−9.605	−9.789	dB
TO_y	0.094	−0.969	1.969	0.031	0.469	0.906	0.594	0.031	0.469	m
scenario S_3: $\mathrm{IRW}_x \simeq 0.555\,\mathrm{m}$, $\mathrm{PSLR}_x \simeq -13.249\,\mathrm{dB}$, $\mathrm{ISLR}_x \simeq -9.685\,\mathrm{dB}$, $\mathrm{TO}_x \simeq 0.018\,\mathrm{m}$										
IRW_y	1.045	0.513	0.514	0.513	0.514	0.516	0.513	0.513	0.514	m
PSLR_y	−0.004	−11.213	−13.255	−11.213	−13.255	−13.191	−11.24	−11.24	−13.257	dB
ISLR_y	1.095	−9.268	−9.897	−9.268	−9.897	−9.779	−9.288	−9.288	−9.898	dB
TO_y	−9.219	−0.031	0.219	−0.031	0.219	−0.031	−0.031	−0.031	0.219	m
scenario S_4: $\mathrm{IRW}_x \simeq 0.555\,\mathrm{m}$, $\mathrm{PSLR}_x \simeq -13.25\,\mathrm{dB}$, $\mathrm{ISLR}_x \simeq -9.687\,\mathrm{dB}$, $\mathrm{TO}_x \simeq 0.018\,\mathrm{m}$										
IRW_y	0.514	0.515	0.539	0.515	0.539	0.514	0.515	0.515	0.539	m
PSLR_y	−12.996	−11.697	−9.965	−11.697	−9.965	−13.096	−11.709	−11.709	−9.965	dB
ISLR_y	−9.615	−9.591	−7.163	−9.591	−7.163	−9.878	−9.61	−9.61	−7.163	dB
TO_y	−0.031	0.031	0.469	0.031	0.469	−0.031	0.031	0.031	0.469	m

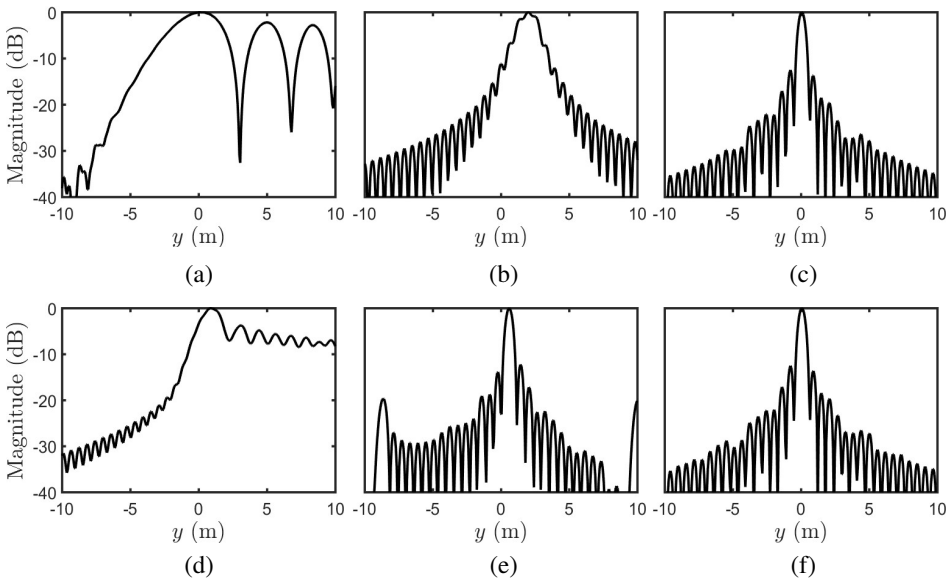

Figure 6. Profiles along y axis of the reconstructed images in scenario S_2, with strategy (a) I-1, (b) II-2, (c) III-1, (d) III-3, (e) R-1 and (f) R-2.

Figure 6 shows the profiles along y axis of the reconstructed image in scenario S_2. Strategies I-1 and III-3 do not work well by similar reasons mentioned in scenario S_1. Strategy II-2 does not work well, either. Strategies III-1 and R-2 outperform the other strategies. The results with strategies II-1,

III-2 and R-3 appear similar to those with strategies III-1 and R-2, except the reconstructed target is offset in the y direction by 0.5 to 1 m, as listed in Table 2. The results with strategy R-1 appear similar to those with strategies III-1 and R-2, except the reconstructed target is offset in the y direction by 0.594 m and has higher ISLR by about 1 dB, as listed in Table 2.

Figure 7 shows the profiles along y axis of the reconstructed image in scenario S_3. The phase coefficient $\tilde{\gamma}(\eta)$, derived by using (26), is close to zero, hence the third-order compensation filter, $H_{c3}(\eta)$, is approximately equal to unity. This implies that strategies III-1, III-2 and R-2 reduce to strategies II-1, II-2 and R-1, respectively.

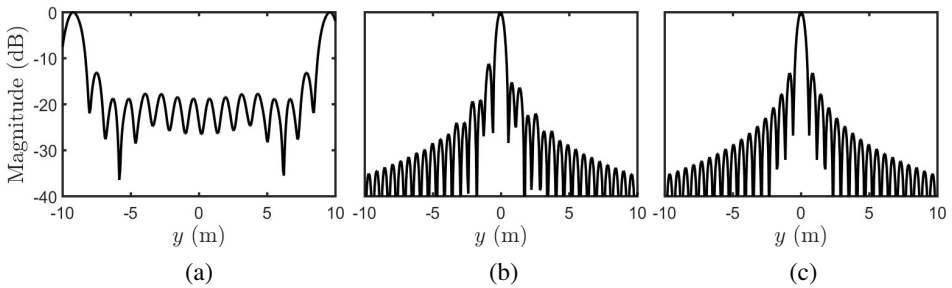

Figure 7. Profiles along y axis of the reconstructed images in scenario S_3, with strategy (a) I-1, (b) II-1 and (c) III-3.

Strategy I-1 does not work well by similar reasons mentioned in scenario S_1. Strategy III-3 works well because $\tilde{\gamma}(\eta)$ is zero, hence possible accumulation error from triple integration becomes negligible. Strategies II-1, III-1, III-3, R-1 and R-2 outperform the other strategies. The results with strategies II-2, III-2 and R-3 look similar to those with strategies II-1, III-1, III-3, R-1 and R-2, except the reconstructed target is offset in the y direction by 0.219 m, as listed in Table 2.

Figure 8 shows the profiles along y axis of the reconstructed image in scenario S_4. Similar to scenario S_3, strategies II-1, III-1, III-3, R-1 and R-2 work well. The results with strategies II-2, III-2 and R-3 appear similar to those with strategies II-1, III-1, III-3, R-1 and R-2, except the reconstructed target is offset in the y direction by 0.469 m and has a higher ISLR of about 3 dB, as listed in Table 2. It is interesting to notice that strategy I-1 works well in this scenario.

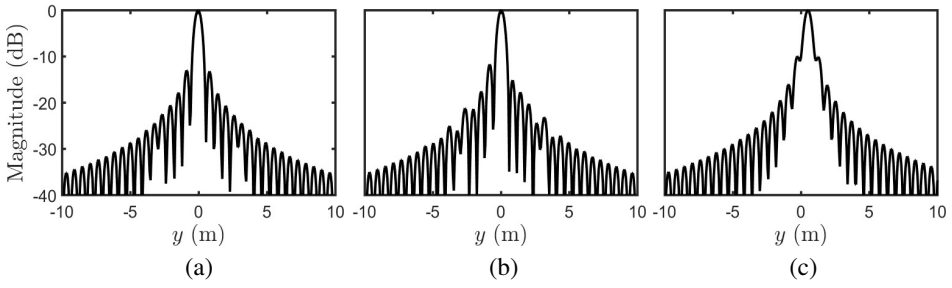

Figure 8. Profiles along y axis of the reconstructed images in scenario S_4, with strategy (a) I-1, (b) II-1 and (c) II-2.

In summary, strategies III-1 and R-2 work satisfactorily in all these four scenarios. In addition, strategy R-2 is more efficient than strategy III-1 in deriving the slow-time profiles of phase coefficients.

The robustness of strategies III-1 and R-2 are further tested under two types of noises. The first type is a Gaussian noise added to the received baseband signal $s_{\mathrm{rb}}(\tau, \eta)$ to demonstrate the immunity of these two strategies to signal noise. Under scenario S_1 for example, with signal-to-noise ratio (SNR) equal to 10, 3 and 0 dB, respectively, the reconstructed images appear almost unaffected by the noise.

The second type of noise is added to the flight-path to simulate platform jittering, which may be caused by turbulence. Under scenario S_1, a Gaussian noise is added to r_s at each η, with SNR equal

to 40, 30 and 20 dB, respectively. The reconstructed images by using strategies III-1 and R-2 become slightly blurred. Note that at SNR = 20 dB, the change of r_s over one slow-time interval $\Delta\eta = 41.67$ ms is on the order of 0.08 m, equivalent to an instantaneous velocity of 192 m/s. In other words, the platform changes its cross-track position by a relatively large amount of 0.08 m as it flies over a distance of 0.0625 m. Similarly, at SNR = 40 dB, the platform changes its cross-track position by 0.008 m when it flies over 0.0625 m.

8. CONCLUSION

Nine different strategies are proposed to compensate cross-track motion errors in synthetic aperture radar (SAR) imaging, by estimating the phase coefficients of the phase history. Four different scenarios are designed to compare the performance of these nine strategies in terms of spatial resolution, PSLR, ISLR and target offset to better understand the pros and cons of these strategies. By simulations over these four scenarios, the reconstructed images show similar characteristics in the cross-track direction, but in some scenarios, quite different characteristics in the along-track direction. Strategies III-1 and R-2 turn out to be most robust in all these four scenarios. In addition, strategy R-2 is more efficient than strategy III-1 in deriving the slow-time profiles of phase coefficients.

REFERENCES

1. Kennedy, T. A., "A technique for specifying navigation system performance requirements in SAR motion compensation applications," *IEEE Position Location Navigation Symp.*, 118–126, Las Vegas, NV, USA, Mar. 1990.
2. Buckreuss, S., "Motion compensation for airborne SAR based on inertial data, RDM and GPS," *IEEE Geosci. Remote Sensing Symp.*, Vol. 4, 1971–1973, Pasadena, CA, USA, Aug. 1994.
3. Moreira, A. and Y. Huang, "Airborne SAR processing of highly squinted data using a chirp scaling approach with integrated motion compensation," *IEEE Trans. Geosci. Remote Sensing*, Vol. 32, No. 5, 1029–1040, Sep. 1994.
4. Moreira, A., J. Mittermayer, and R. Scheiber, "Extended chirp scaling algorithm for air- and spaceborne SAR data processing in stripmap and scanSAR imaging modes," *IEEE Trans. Geosci. Remote Sensing*, Vol. 34, No. 5, 1123–1136, Sep. 1996.
5. Li, Y.-P., M.-D. Xing, and Z. Bao, "A new method of motion error extraction from radar raw data for SAR motion compensation," *IEEE CIE Int. Conf. Radar*, Shanghai, China, Oct. 2006.
6. Xing, M.-D., X.-W. Jiang, R.-B. Wu, F. Zhou, and Z. Bao, "Motion compensation for UAV SAR based on raw radar data," *IEEE Trans. Geosci. Remote Sensing*, Vol. 47, No. 8, 2870–2883, Aug. 2009.
7. Zhang, L., G.-Y. Wang, Z.-J. Qiao, and H.-X. Wang, "Azimuth motion compensation with improved subaperture algorithm for airborne SAR imaging," *IEEE J. Select. Topics Appl. Earth Observ. Remote Sensing*, Vol. 10, No. 1, 184–193, Jan. 2017.
8. Prats, P., K. A. C. Macedo, A. Reigber, R. Scheiber, and J. J. Mallorqui, "Comparison of topography- and aperture-dependent motion compensation algorithms for airborne SAR," *IEEE Geosci. Remote Sensing Lett.*, Vol. 4, No. 3, 349–353, Jul. 2007.
9. Macedo, K. A. C. and R. Scheiber, "Precise topography- and aperture-dependent motion compensation for airborne SAR," *IEEE Geosci. Remote Sensing Lett.*, Vol. 2, No. 2, 172–176, Apr. 2005.
10. Perna, S., V. Zamparelli, A. Pauciullo, and G. Fornaro, "Azimuth-to-frequency mapping in airborne SAR data corrupted by uncompensated motion errors," *IEEE Geosci. Remote Sensing Lett.*, Vol. 10, No. 6, 1493–1497, Nov. 2013.
11. Zheng, X., W. Yu, and Z. Li, "A novel algorithm for wide beam SAR motion compensation based on frequency division," *IEEE Int. Geosci. Remote Sensing Symp.*, 3143–3146, Denver, Colorado, USA, Aug. 2006.

12. Li, Y.-L., X.-D. Liang, C.-B. Ding, L.-J. Zhou, and Q. Ding, "Improvements to the frequency division-based subaperture algorithm for motion compensation in wide-beam SAR," *IEEE Geosci. Remote Sensing Lett.*, Vol. 10, No. 5, 1219–1223, Sep. 2013.
13. Chen, Y.-C., G. Li, Q. Zhang, Q.-J. Zhang, and X.-G. Xia, "Motion compensation for airborne SAR via parametric sparse representation," *IEEE Trans. Geosci. Remote Sensing*, Vol. 55, No. 1, 551–562, Jan. 2017.
14. Gu, F.-F., Q. Zhang, L. Chi, Y.-A. Chen, and S. Li, "A novel motion compensating method for MIMO-SAR imaging based on compressed sensing," *IEEE Sensors J.*, Vol. 15, No. 4, 2157–2165, Apr. 2015.
15. Fornaro, G., "Flight path deviations in airborne SAR: Analysis and compensation," *IEEE Trans. Aerosp. Electron. Syst.*, Vol. 35, No. 3, 997–1009, Jul. 1999.
16. Fornaro, G., G. Franceschetti, and S. Perna, "On center-beam approximation in SAR motion compensation," *IEEE Geosci. Remote Sensing Lett.*, Vol. 3, No. 2, 276–279, Apr. 2006.
17. Zhang, L., Z. Qiao, M.-D. Xing, L. Yang, and Z. Bao, "A robust motion compensation approach for UAV SAR imagery," *IEEE Trans. Geosci. Remote Sensing*, Vol. 50, No. 8, 3202–3218, Aug. 2012.